Generation of elliptically polarized attosecond pulses in mixed gases

Chunyang Zhai ☉,[1] Xiaosong Zhu,[2,*] Jie Long,[2] Renzhi Shao ☉,[2] Yinfu Zhang,[2] Lixin He,[2] Qingbin Tang,[1] Yingbin Li,[1,†] Pengfei Lan,[2,‡] Benhai Yu,[1] and Peixiang Lu ☉[3]

[1]*College of Physics and Electronic Engineering, Xinyang Normal University, Xinyang 464000, China*
[2]*Wuhan National Laboratory for Optoelectronics and School of Physics, Huazhong University of Science and Technology, Wuhan 430074, China*
[3]*Guangdong Intelligent Robotics Institute, Dongguan 523808, China*

We propose and theoretically demonstrate a scheme to generate elliptically polarized attosecond pulses with mixed gases. As the harmonic radiations from different gases with opposite orbital parity interfere destructively for one helicity component and constructively for the other, the high-order harmonics from the mixture exhibit large ellipticity with the same helicity in a wide spectral range. Hence, highly elliptically polarized attosecond pulses can be generated from the mixed gases and the ellipticity can be tuned by controlling the mixing ratio and the molecular alignment angle. Furthermore, this interference effect is only related to the features of the mixed gases such as the structure and orbital symmetry of the molecules and atoms. The polarization control is independent of the temporal profile manipulation of the attosecond pulses by shaping the driving field. Consequently, our work paves an effective and convenient way to produce elliptically polarized isolated attosecond pulses with mixed gases by optimizing the polarization and temporal profile individually.

I. INTRODUCTION

High-order-harmonic generation (HHG) has become a major tool for producing attosecond pulses of extreme ultraviolet and soft x-ray light using tabletop-scale lasers. Attosecond pulses have many important applications in physics, chemistry, biology, medicine, and information technology [1–8]. In particular, the availability of circularly polarized attosecond pulses in the form of isolated attosecond pulses (IAPs) and attosecond pulse trains (APTs) would enable attosecond-resolved measurements of chirality and magnetization [9–12]. The HHG process is a laser-induced recollision process that can be well understood by the semiclassical three-step model [13]. When the atom or molecule is driven by an intense laser field, an electron is first lifted to the continuum through tunneling ionization. Then, the subsequent motion of the electron is governed classically by the oscillating electric field. Finally, the electron returns and recombines with the parent ion with emitting high-order harmonics. According to the three-step model, the freed electron returns to the parent ion along the laser polarization direction when driven by linearly polarized laser fields. When the polarization of the driving laser field changes from linear to circular, the electron will be driven away from its parent by the transverse field component so that the HHG efficiency falls off rapidly [14–16]. The ellipticity-dependent HHG efficiency presents a roadblock in bright circularly polarized HHG and attosecond-pulse generation.

To obtain circularly or elliptically polarized high-order harmonics and attosecond pulses, a lot of effort is devoted nowadays to both theoretical and experimental studies [17]. One major scenario is to modify the HHG process by using two-dimensional driving laser fields [18–32]. The bichromatic counter-rotating circularly polarized (BCCP) field and the orthogonal two-color (OTC) field have been experimentally demonstrated to be effective tools for circularly and elliptically polarized HHG. In the BCCP method [22–25], the synthesized field consists of a circularly polarized fundamental field and its second harmonic field with opposite rotation direction. For an isotropic target, the system has a threefold symmetry where the $3m$-order (m is a positive integer) harmonics are prohibited according to the selection rule [33,34]. At the same time, the $(3m+1)$-order harmonics are circularly polarized with the same helicity as the fundamental field, and the $(3m-1)$-order harmonics are circularly polarized with the same helicity as the second harmonic field. This can also be understood based on the conservation of angular momentum in the HHG process [22]. Besides the BCCP field, the OTC method is another widely used two-color scheme to generate elliptically polarized HHG [26–28]. By modulating the OTC field, one can obtain ellipticity-tunable high-order harmonics, but the odd- and even-order harmonics have opposite helicity. Both the BCCP fields and OTC fields are effective to generate individual elliptically polarized harmonics. However, it is hard to synthesize highly elliptically polarized attosecond pulses due to the different helicity of the neighboring harmonics. Another important type of scenario to generate circularly or elliptically polarized high-order harmonics and attosecond pulses is to prepare specific targets. For example, prealigned molecules can cause the emission of elliptically polarized

*zhuxiaosong@hust.edu.cn
†liyingbin2008@163.com
‡pengfeilan@hust.edu.cn

high-order harmonics [35,36]. In this approach, only a one-color linearly polarized field is required, but the measured ellipticity is not large. In addition, the presence of a ring current in the medium can also produce elliptically polarized HHG [37–40]. Yet the preparation of current-carrying states is challenging in experiment at present [37]. In addition to the above two types of scenarios, some other methods can also produce circularly or elliptically polarized HHG in experiment. Vodungbo *et al.* implemented a four-reflector phase shifter to convert the high-order harmonics from linear polarization to circular polarization [41]. In addition, noncollinear driving lasers have also been adopted to produce elliptically polarized HHG [42–45]. When both driving beams overlap in time and space, the polarization of the synthesized field in the interaction region rotates along the transverse position, forming a "rotating polarization grating." Consequently, one can obtain polarization-controlled high-order harmonics in the far field at different divergence angles. Recently, Azoury *et al.* reported a new scheme to produce extreme-ultraviolet radiation with arbitrary ellipticity based on two individual, phase-locked, and orthogonally polarized HHG sources [46]. The basic principles of these schemes are straightforward, but the experimental operation usually requires attosecond accuracy and sophisticated techniques with formidable challenges. In view of the above, there are still obstacles to produce highly elliptically polarized HHG with the same helicity in a broad spectral range, i.e., to produce highly elliptically polarized attosecond pulses.

In the present work, we demonstrate a scheme to produce elliptically polarized attosecond pulses based on the interaction between one-color linearly polarized driving fields and mixed gases. By mixing atomic and molecular gases with opposite orbital parity, the resulting high-order harmonics with one helicity interfere constructively, while those with the other helicity interfere destructively, yielding elliptically polarized attosecond pulses. Furthermore, we show that elliptically polarized IAPs can be produced in mixed gases driven by a few-cycle linearly polarized field. The ellipticity of the IAPs is insensitive to the waveform of the driving laser field, i.e., the polarization and the temporal profile of the IAPs generated by the mixed gases scheme can be individually controlled.

II. THEORETICAL METHOD

In order to demonstrate our scheme, we calculate the high-order-harmonic radiation based on the Lewenstein model [47]. The time-dependent dipole moment is described as (atomic units are used, unless otherwise noted) [47–49]

$$
\begin{aligned}
D(t) = i \int_{-\infty}^{t} dt' & \left[\frac{\pi}{\xi + i(t-t')/2} \right]^{3/2} \\
& \times \mathbf{d}[\mathbf{p}_s(t',t) - \mathbf{A}(t')]\mathbf{d}^*[\mathbf{p}_s(t',t) - \mathbf{A}(t)] \\
& \times e^{-iS(t',t)} \mathbf{E}(t')g(t') + \text{c.c.}
\end{aligned} \tag{1}
$$

Here, $\mathbf{E}(t) = E_0 f(t)\cos(\omega t + \phi)$ is the driving laser field, with E_0, ω, and ϕ the amplitude, frequency, and the carrier-envelope phase (CEP) of the field, respectively. $f(t)$ is the envelope of the laser pulse, ξ is a positive regularization constant, and $g(t')$ is the ground-state amplitude. $S(t',t)$ is the

quasiclassical action and can be written as

$$
S(t',t) = \int_{t'}^{t} dt'' \left\{ \frac{[\mathbf{p}_s(t',t) - \mathbf{A}(t'')]^2}{2} + I_p \right\}, \tag{2}
$$

where I_p is the ionization potential of the gas target. $\mathbf{p}_s(t',t)$ and $\mathbf{A}(t)$ are the stationary momentum and corresponding vector potential, which are given by

$$
\mathbf{p}_s(t',t) = \frac{1}{t-t'} \int_{t'}^{t} \mathbf{A}(t'')dt'' \tag{3}
$$

and

$$
\mathbf{A}(t) = -\int_{-\infty}^{t} \mathbf{E}(t')dt'. \tag{4}
$$

$\mathbf{d}[\mathbf{p}_s(t',t) - \mathbf{A}(t')]$ and $\mathbf{d}^*[\mathbf{p}_s(t',t) - \mathbf{A}(t)]$ denote the dipole matrix element for the ionization transition dipole and recombination transition dipole, which are characterized by the electron momentum $\mathbf{p} = \mathbf{p}_s - \mathbf{A}$. Within the strong-field approximation [47], the transition dipole moment for the bound-free transition is given by

$$
\mathbf{d}(\mathbf{p}) = \langle e^{-i\mathbf{p}\cdot\mathbf{r}} | \mathbf{r} | \Psi \rangle, \tag{5}
$$

where Ψ is the ground state of the target atom or molecule, which is obtained by an *ab initio* calculation in the GAUSSIAN09 code [50]. Then the harmonic radiation is proportional to the time-dependent dipole acceleration $\ddot{D}(t)$ and the harmonic spectrum is obtained from the Fourier transform of $\ddot{D}(t)$:

$$
I^{\text{hhg}}(q) = |\mathbf{E}^{\text{hhg}}(q)|^2 \tag{6}
$$

and

$$
\mathbf{E}^{\text{hhg}}(q) = \int \ddot{D}(t) e^{-iq\omega t} dt, \tag{7}
$$

where q is the harmonic order.

To analyze the results, we project the radiation field either on the polarization vectors parallel and perpendicular to the driving laser field or on the right- and left-rotating polarization vectors. The right-rotating component $\mathbf{E}_R^{\text{hhg}}$ and left-rotating component $\mathbf{E}_L^{\text{hhg}}$ are given by

$$
\mathbf{E}_R^{\text{hhg}} = \left(\mathbf{E}_x^{\text{hhg}} + i\mathbf{E}_y^{\text{hhg}} \right)/\sqrt{2} \tag{8}
$$

and

$$
\mathbf{E}_L^{\text{hhg}} = \left(\mathbf{E}_x^{\text{hhg}} - i\mathbf{E}_y^{\text{hhg}} \right)/\sqrt{2}, \tag{9}
$$

where $\mathbf{E}_x^{\text{hhg}}$ and $\mathbf{E}_y^{\text{hhg}}$ are the parallel and perpendicular components of $\mathbf{E}^{\text{hhg}}$, respectively. The ellipticity ε of high-order harmonics is determined by the amplitude ratio $r = |\mathbf{E}_y^{\text{hhg}}|/|\mathbf{E}_x^{\text{hhg}}|$ and the phase difference $\delta = \arg(\mathbf{E}_y^{\text{hhg}}) - \arg(\mathbf{E}_x^{\text{hhg}})$,

$$
\varepsilon = \tan\left(\tfrac{1}{2}\text{asin}\{\sin[2\text{atan}(r)]\sin(\delta)\} \right). \tag{10}
$$

The polarization state of high-order harmonics can also be characterized by the degree of circular polarization [20,51],

$$
\zeta = \frac{I_R - I_L}{I_R + I_L}, \tag{11}
$$

where I_R and I_L are the intensity of the right- and left-rotating components, which can be read as

$$I_R = \left| \mathbf{E}_R^{\text{hhg}} \right|^2 \tag{12}$$

and

$$I_L = \left| \mathbf{E}_L^{\text{hhg}} \right|^2. \tag{13}$$

Here, the degree of circular polarization ζ is connected with the ellipticity ε by the formula [20]

$$\zeta = \frac{2\varepsilon}{1 + \varepsilon^2}. \tag{14}$$

III. RESULTS AND DISCUSSIONS

According to the three-step model for the HHG process [13], the final recombination step leads to the emission of high-order harmonics. The phase difference of the high-order-harmonics radiation from different polarization components or different ground states is mainly contributed by that of the recombination dipole moment, if the ionization potentials I_p of the ground states are the same [5,52–57]. To illustrate the mechanism for the generation of elliptically polarized high-order harmonics, a schematic diagram for the recombination dipole moment based on the rotation vector method is shown in Fig. 1, where complex values are represented as vectors in the complex plane.

To generate elliptically polarized high-order harmonics from linear driving fields, prealigned molecules are generally used to obtain a harmonic component perpendicular to the polarization direction of the driving field because a nonzero perpendicular component of the recombination dipole moment emerges due to the nonisotropic molecular structure. The vectors $\overrightarrow{OC}$ and $\overrightarrow{CD}$ in Fig. 1 represent the parallel d_x^m and perpendicular d_y^m components of the recombination dipole
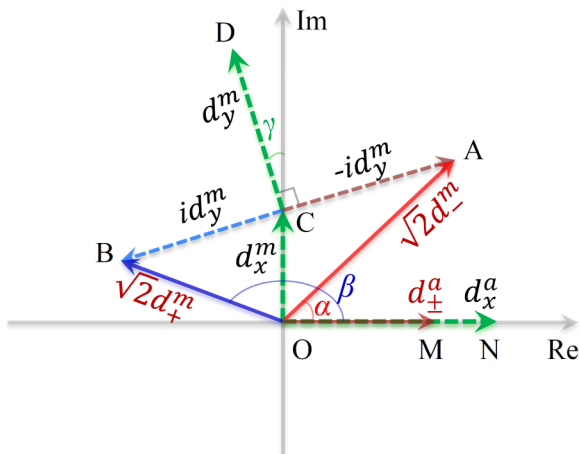

FIG. 1. Schematic for the interference in mixed gases based on the rotation vector method, where complex values are represented as vectors in the complex plane. The horizontal axis corresponds to the real axis and the vertical axis corresponds to the imaginary axis. $d_{x,y}^{m,a}$ is the recombination dipole moment projected onto the x/y direction. $d_\pm^{m,a} = (d_x^{m,a} \pm i d_y^{m,a})/\sqrt{2}$ is the right- and left-rotating component. The superscripts a and m represent the atom and molecule, respectively.

moment of the molecule. γ is the phase difference between d_x^m and d_y^m. Here, we are concerned with the cases where γ is small, which is generally true in the high-energy region where the continuum states can be well described by plane waves. With the small γ, highly elliptically polarized high-order harmonics cannot be obtained from the molecules alone. This can be intuitively understood in Fig. 1: The superposition of $d_{x/y}^m$ gives the right-rotating component $d_+^m = \frac{1}{\sqrt{2}}(d_x^m + i d_y^m)$ corresponding to $\frac{1}{\sqrt{2}}\overrightarrow{OB} = \frac{1}{\sqrt{2}}(\overrightarrow{OC} + \overrightarrow{CB})$ and the left-rotating component $d_-^m = \frac{1}{\sqrt{2}}(d_x^m - i d_y^m)$ corresponding to $\frac{1}{\sqrt{2}}\overrightarrow{OA} = \frac{1}{\sqrt{2}}(\overrightarrow{OC} + \overrightarrow{CA})$. The length $|\overrightarrow{OB}| \approx |\overrightarrow{OA}|$ when γ is small, i.e., the amplitudes of the right- and left-rotating harmonic components, are nearly the same, leading to a low ellipticity [see Eqs. (11) and (14)].

To increase the ellipticity, one should increase the difference between the amplitudes of the right- and left-rotating components. This can be realized by introducing selective interference so that one rotating component interferes destructively, while the other one interferes constructively [40]. We propose that the interference can be introduced by mixing the molecular target with another isotropic target, e.g., an atomic gas, with opposite orbital parity. Herein, without loss of generality, we consider a mixture of molecules with even orbital parity and atoms with odd orbital parity. For the atomic target, there is only the parallel component, i.e., $d_y^a = 0$. Therefore, both the right- and left-rotating components satisfy $d_\pm^a = \frac{1}{\sqrt{2}} d_x^a$ as denoted by $\overrightarrow{OM} = \frac{1}{\sqrt{2}}\overrightarrow{ON}$. Based on the orbital parities of the two targets, the phase of the recombination dipole moment for the molecular target is near $\pi/2$ and that for the atomic target is near 0 [58]. When the perpendicular component d_y^m for the molecule is comparable to or even larger than that of the parallel component d_x^m, the phase difference between the right-rotating component d_+^m and the left-rotating component d_-^m, i.e., $\angle AOB$ in Fig. 1, is larger than $\pi/2$. In this case, the phase difference between right-rotating components from the molecule and atom, i.e., β, is close to π, resulting in destructive interference. On the contrary, the phase difference between left-rotating components from the molecule and atom, i.e., α, is close to 0, resulting in constructive interference. According to the above discussion, the mixed-gas approach with one molecular target and one atomic target works when (1) the aligned molecules can generate a perpendicular component of high-order harmonics so that the right- and left-rotating components are (approximately) out of phase, and (2) the molecule and atom have opposite orbital parity.

In the proof-of-principle study, we consider a mixture of N_2 and Ar. The N_2 molecule and Ar atom have nearly the same ionization potential I_p that match the intrinsic phase due to the electron propagation [54,55]. As is shown in the insets of Fig. 2, the Ar atom and N_2 molecule have opposite orbital parity. The ground states for the Ar atom are the $3p$ orbitals with odd parity and that for N_2 molecule is the $3\sigma_g$ orbital with even parity, i.e., the highest occupied molecular orbital (HOMO) of N_2. We first calculate the high-order harmonics from Ar and N_2 separately. The driving laser field is a one-color linearly polarized field. Its envelope is trapezoidal with
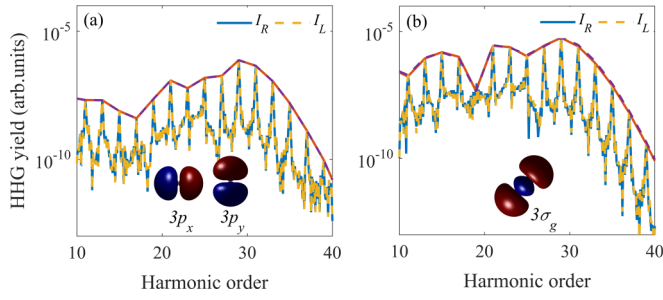
FIG. 2. High-order-harmonic spectra from (a) Ar and (b) N_2. The blue solid and yellow dashed lines represent the harmonic spectra for the right-rotating component I_R and the left-rotating component I_L, respectively. The insets are the ground states of the Ar atom and N_2 molecule.

a two-cycle rising and a two-cycle falling edge and a six-cycle plateau. The wavelength and intensity of the laser field are 800 nm and 1.5×10^{14} W/cm^2, respectively. Figures 2(a) and 2(b) present the high-order-harmonic spectra from Ar and N_2 aligned at $45°$. Figure 2(a) shows that the left- and right-rotating spectra are exactly the same, which indicates that the polarization of the high-order-harmonic radiation from Ar is linear. Although the left- and right-rotating components from N_2 are slightly different in the cutoff region, as shown in Fig. 2(b), it is too small to synthesize elliptically polarized attosecond pulses. The result is in agreement with the previous works [35,36,52,59]. Considering a mixture of Ar and N_2 gases; the emission of high-order harmonics is the coherent sum of the emission from both species [55–57,60,61]. In the simulation, we set the mixing ratio of N_2:Ar to 0.25:1 to balance the intensity of high-order harmonics generated from the two targets. As is shown in Figs. 3(a) and 3(b), the left- (right-) rotating components are almost equal to each other above the 21st-order harmonic. The relative phase $\Delta\phi_R$ between the right-rotating components from Ar and N_2 is close to π above the 21st-order harmonic [see Fig. 3(c)], leading to the destructive interference for the right-rotating components. On the contrary, the relative phase $\Delta\phi_L$ between the left-rotating components is close to 0 above the 21st-order harmonic [see Fig. 3(c)], leading to constructive interference. This is consistent with the discussions in Fig. 1. Both the destructive interference of the right-rotating components and the constructive interference of the left-rotating components occur in a wide spectral range. As a result, the HHG of Ar-N_2 mixed gases exhibits a large intensity difference between the left- and right-rotating components in a broad bandwidth, as shown in Fig. 3(d). It has been proved that the results based on the Lewenstein model agree qualitatively with those of the time-dependent Schrödinger equation (TDSE) [62]. We confirmed the validity of the mixed-gases scheme in the TDSE calculations as well, including the interference effect due to the relative phase relation for the two targets and the ellipticity of the total high-order harmonics (see more details in the Appendix).

Next, we consider the HHG from mixed gases for various molecular alignment. Figure 4 shows the ellipticity of high-order harmonics from Ar-N_2 mixed gases versus N_2 molecular alignment angle θ. One can see that the helicity is
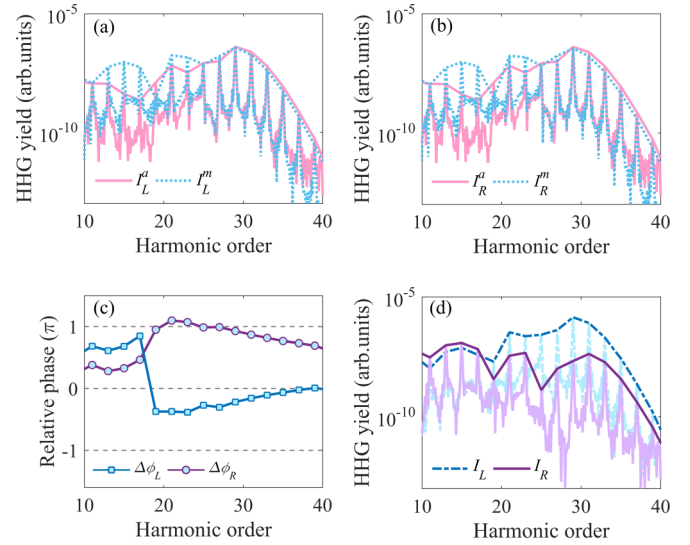

FIG. 3. High-order-harmonic spectra for the (a) left- and (b) right-rotating components from Ar (red solid lines) and N_2 (blue dashed lines), respectively. (c) The relative phase between high-order-harmonic radiation from Ar and N_2 for the left-rotating harmonic components ($\Delta\phi_L$, blue squares) and the right-rotating harmonic components ($\Delta\phi_R$, purple circles). (d) High-order-harmonic spectra from Ar-N_2 mixed gases for the left-rotating component (I_L, blue dash-dotted line) and right-rotating component (I_R, purple solid line), respectively.

antisymmetric with respect to $\theta = 90°$. Due to the symmetry of the HOMO of N_2, the perpendicular component of the harmonic radiation is much smaller than the parallel component when the N_2 molecule is aligned at about $\theta = 0°/180°$ and $\theta = 90°$. As a consequence, the ellipticities are near 0 when the N_2 molecule is parallel or perpendicular to the driving laser field, as shown in Fig. 4. However, the ellipticity increases at intermediate angles up to $\varepsilon = 0.88$, as the perpendicular component from N_2 increases. Furthermore, the ellipticity remains large with the same helicity over
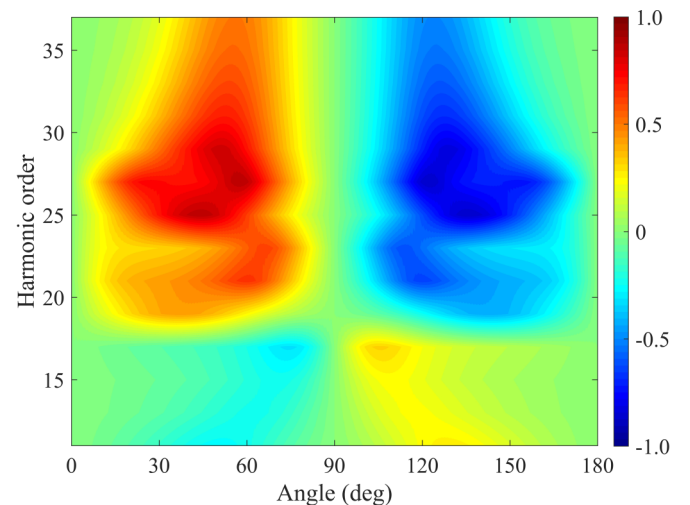

FIG. 4. The ellipticity of high-order harmonics from mixed gases as a function of harmonic order and the molecular alignment angle.
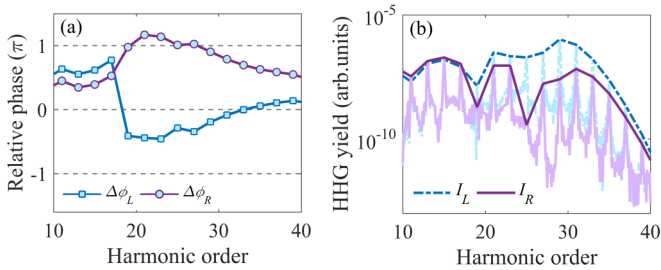
FIG. 5. The results considering the molecular alignment distribution. (a) The relative phase between high-order-harmonic radiation from Ar and N_2 for the left-rotating harmonic components ($\Delta\phi_L$, blue squares) and right-rotating harmonic components ($\Delta\phi_R$, purple circles). (b) High-order-harmonic spectra from Ar-N_2 mixed gases for the left-rotating component (I_L, blue dash-dotted line) and right-rotating component (I_R, purple solid line), respectively. The laser parameters are the same as those in Fig. 3.
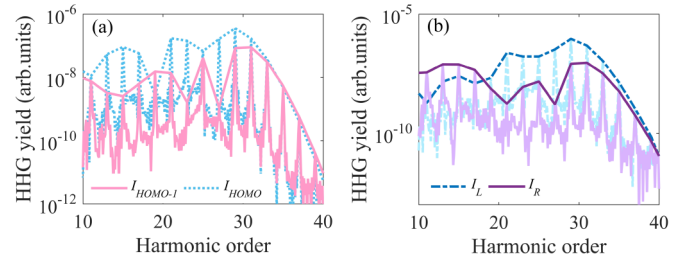

FIG. 6. The results considering the multiple orbital contribution. (a) High-order-harmonic spectra from HOMO (blue dashed lines) and HOMO-1 (red solid lines) of N_2. (b) High-order-harmonic spectra from Ar-N_2 mixed gases for the left-rotating component (I_L, blue dash-dotted line) and the right-rotating component (I_R, purple solid line), with the contributions of both HOMO and HOMO-1 considered for N_2. The laser parameters are the same as those in Fig. 3.

a wide alignment angle range from $\theta = 20°(110°)$ to $\theta = 70°(160°)$ for the harmonics above the 21st order. Note that the high-order-harmonic signal measured in the macroscopic molecular ensemble in the laboratory frame is a convolution of the single molecular signal with the alignment distribution [57,63,64]. Therefore, it is necessary to consider the molecular alignment distribution to exclude the ambiguity due to the imperfect alignment. According to [6,65], we calculate the molecular alignment distribution. The alignment degree $\langle\cos^2\theta\rangle = 0.65$ is used in our simulation, which can be easily achieved in the experiment [63,64]. Then we calculate the results considering the molecular alignment distribution shown in Fig. 5. In comparison with the results of perfect molecular alignment, one can see that the relative phases for the two targets are also close to 0 and π, respectively [see Figs. 3(c) and 5(a)]. The high-order harmonics from the mixture are still dominantly contributed by the left-rotating component in the wide spectral range, although the difference between the left- and right-rotating components is slightly decreased due to the imperfect alignment [see Figs. 3(d) and 5(b)]. The corresponding ellipticities of the harmonics above the 21st order dropped by about 0.1.

To more precisely study the ellipticity of high-order harmonics from the mixture of Ar and N_2, the multiple orbital contribution of the molecule should be taken into account. It has been shown that HOMO-1, which has the same parity as the $3p$ orbital, may contribute significantly to the harmonics in the cutoff region for N_2 [66]. In Fig. 6(a), we compare the contributions of HOMO and HOMO-1 of N_2. The harmonic component contributed from HOMO-1 is ~ 1–2 orders of magnitude lower than that from HOMO in the plateau region. However, the contributions from the two orbitals are comparable in the cutoff region. Consequently, the influence of HOMO-1 on the ellipticity of harmonics can be ignored, except for the cutoff region [see Fig. 6(b)]. Meanwhile, as the harmonic intensity in the cutoff region is much lower than that in the plateau region, its influence on the synthesized attosecond pulse is limited. As a result, only the contribution of HOMO is considered in the following.

To confirm the robustness of the generation of elliptically polarized high-order harmonics with the mixed-gas approach,

we simulate the HHG from Ar-N_2 mixed gases with various laser parameters. In the simulation, the N_2 molecule is aligned at 45°. The intensity of the driving laser increases from 1×10^{14} to 2×10^{14} W/cm². The result is shown in Fig. 7. One can see that the cutoff of the high-order harmonics is extended remarkably. In the broad spectral range, the ellipticity of high-order harmonics is high and the helicity is always the same. Owing to the quantum path interference in HHG [67], the periodic modulation of high-order harmonics is also clearly visible in our results. The robustness of the mixed-gases scheme is additionally confirmed by simulation of HHG driven by different laser wavelengths.

By taking advantage of the large ellipticity and the same helicity of high-order harmonics in a broad spectral range, the elliptically polarized attosecond pulses can be obtained by superposing the HHG from mixed gases. Figure 8 shows the APT computed by inverse Fourier transform of the corresponding spectra, taking an energy window from the 25th-order harmonic up to the 39th-order harmonics. The parameters of the driving laser field and the targets are the same
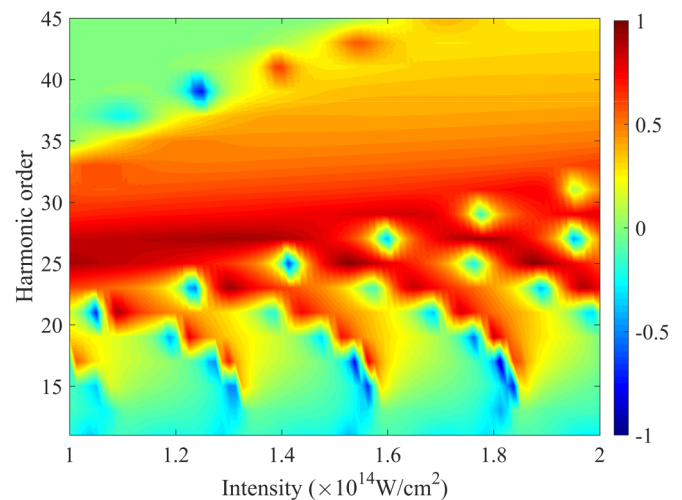

FIG. 7. The ellipticity of high-order harmonics from mixed gases as a function of harmonic order and the intensity of the driving laser field.
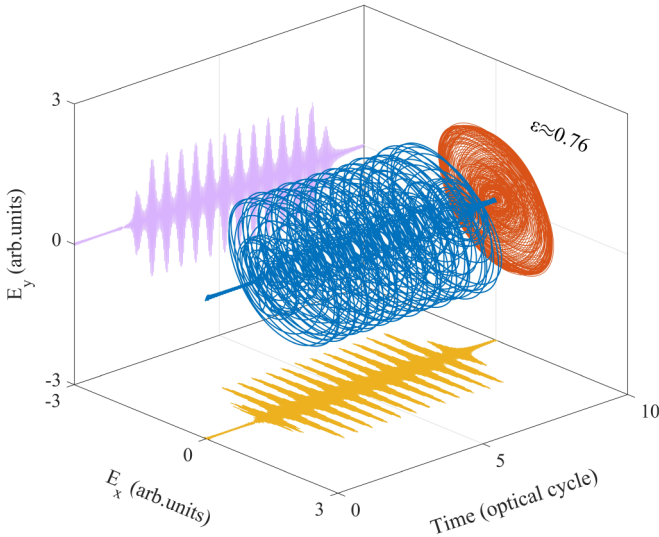
FIG. 8. The three-dimensional plot of the electric field for the synthesized attosecond-pulse train with the high-order harmonics from mixed gases. The ellipticity of the attosecond-pulse train is $\varepsilon \approx 0.76$.

FIG. 9. Results from Ar-N$_2$ mixed gases driven by a few-cycle laser field. (a) The relative phase between high-order-harmonic radiation from Ar and N$_2$ for the left-rotating harmonic components ($\Delta\phi_L$, blue squares) and right-rotating harmonic components ($\Delta\phi_R$, purple circles). (b) High-order-harmonic spectra from Ar-N$_2$ mixed gases for the left-rotating component (I_L, blue dash-dotted line) and right-rotating component (I_R, purple solid line), respectively. (c) Time-frequency distribution of the high-order harmonics under the few-cycle laser field. The color map represents the high-order-harmonic intensity in the logarithmic scale. (d) The three-dimensional plot of the electric field for the synthesized isolated attosecond pulse with the high-order harmonics from mixed gases. The ellipticity of the isolated attosecond pulse is about 0.81 and the pulse duration is about 300 as.

in Fig. 3. The waveform of the three-dimensional electric-field vector (blue), the two orthogonal electric-field components E_x (yellow) and E_y (purple), and the projection on the E_x-E_y plane (orange) are displayed. From the helical structures of the electric-field contour plotted in this three-dimensional image, one can directly see that each attosecond pulse is elliptically polarized. We calculate the ratio of the minor axis to the major axis of the elliptically polarized attosecond field to evaluate the ellipticity of the attosecond pulse. The ellipticity of the generated APT is about 0.76.

In addition, we also consider producing highly elliptically polarized IAPs by using few-cycle driving laser fields. In the simulation, a Gaussian envelope for the laser pulse whose full width at half maximum (FWHM) is 5 fs is used. The wavelength and intensity of the few-cycle driving laser field are 800 nm and 1.5×10^{14} W/cm^2, respectively. The CEP is set to $\phi = 0.7\pi$. The N$_2$ molecular axis is fixed at 45° relative to the polarization of the driving laser field. Figure 9(a) presents the relative phase between high-order harmonics generated from Ar and N$_2$ for the right-rotating component ($\Delta\phi_R$) and left-rotating component ($\Delta\phi_L$), respectively. One can see that $\Delta\phi_R$ is near π and $\Delta\phi_L$ is near 0 in a wide spectral range. Therefore, the right-rotating components will interfere destructively. On the contrary, the left-rotating components will interfere constructively. As shown in Fig. 9(b), it is obvious that the intensity of the left-rotating component generated from the mixture of Ar and N$_2$ is much larger than that of the right-rotating component above the 21st-order harmonic. The result is in accordance with that of multicycle laser fields [see Figs. 3(c) and 3(d)] and the analysis in Fig. 1. Moreover, the high-order-harmonic spectra exhibit a broadband supercontinuum with a regular modulation structure close to the cutoff region. For a deep insight into the generation of the supercontinuum, we present the time-frequency distribution of the high-order-harmonic spectra in Fig. 9(c). The color map of Fig. 9(c) represents the high-order-harmonic intensity in
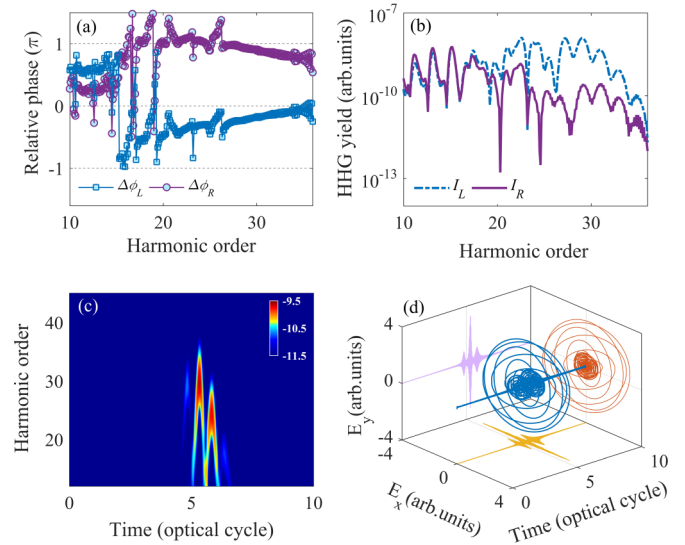
the logarithmic scale. The time-frequency distribution shows that the high-order harmonics above the 25th order are mainly emitted between the 5th and the 5.5th optical cycle. The highest energy of this burst is much higher than those of the adjacent satellite bursts. Therefore, an IAP can be obtained by filtering the high-order harmonics in the supercontinuum. Figure 9(d) shows the IAP computed by inverse Fourier transform of the corresponding spectra, taking an energy window from the 25th-order harmonic up to the 39th-order harmonic. As expected, an IAP is produced. The ellipticity of the generated IAP is $\varepsilon \approx 0.81$ and the pulse duration (FWHM) is $\tau \approx 300$ as. In terms of a physical mechanism, as we have analyzed above, the ellipticity of high-order harmonics and, consequently, the attosecond pulses are only dependent on the atomic and molecular structure, symmetry, and molecular orientation in the mixed-gases scheme. The polarization properties are insensitive to the waveform of the driving laser fields. Therefore, the ellipticity and the temporal profile of the attosecond pulses can be manipulated separately.

IV. CONCLUSIONS

In conclusion, we theoretically demonstrate a mixed-gases scheme for generating elliptically polarized high-order harmonics and attosecond pulses. Benefiting from the interference of high-order harmonics generated from the atomic and

molecular gases which have opposite orbital parity, we obtain elliptically polarized HHG in a broad spectral range. These high-order harmonics have the same helicity, and thus can be used to synthesize highly elliptically polarized attosecond pulses. In the simulation, by using a linearly polarized driving laser field, an APT with an ellipticity of $\varepsilon \approx 0.76$ from Ar-N_2 mixed gases is produced. Further, an IAP with a high ellipticity of $\varepsilon \approx 0.81$ and duration of $\tau \approx 300$ can be obtained with a few-cycle laser field. Since the polarization of the generated high-order harmonics from mixed gases relies on the structure and orbital parity of the atoms and molecules and is insensitive to the waveform of the driving laser, the ellipticity and the temporal profile of the attosecond pulses can be manipulated separately, which provides the possibility of generating large ellipticity without affecting the latter.

APPENDIX: CALCULATION WITH TDSE

Here we describe the details of the calculation with TDSE. We investigate the interaction between the laser fields and the target gases by solving the two-dimensional TDSE,

$$i\frac{\partial}{\partial t}\psi(\mathbf{r}, t) = \hat{H}(\mathbf{r}, t)\psi(\mathbf{r}, t), \tag{A1}$$

where $\hat{H}(\mathbf{r}, t)$ is the Hamiltonian given by

$$\hat{H}(\mathbf{r}, t) = -\frac{1}{2}\nabla^2 + V(\mathbf{r}) + \mathbf{r} \cdot \mathbf{E}(t), \tag{A2}$$

and $V(\mathbf{r})$ is the potential of the system. For the molecule, we employ the effective potential in the form of [68,69]

$$V(\mathbf{r}) = -\sum_j \frac{Z_j^\infty + (Z_j^0 - Z_j^\infty)e^{-(\mathbf{r}-\mathbf{R}_j)^2/\sigma_j^2}}{\sqrt{a_j^2 + (\mathbf{r} - \mathbf{R}_j)^2}}. \tag{A3}$$

The subscript $j = 1, 2$ labels the nucleus of N_2. Z_j^0 and Z_j^∞ denote the bare charge and the effective nuclear charge as seen
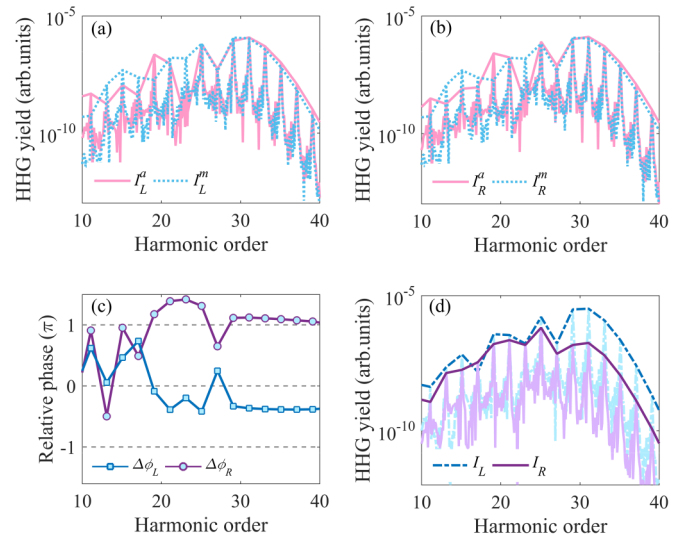

FIG. 10. Results of the calculation with TDSE. High-order-harmonic spectra for the (a) left- and (b) right-rotating components from Ar (red solid lines) and N_2 (blue dashed lines), respectively. (c) The relative phase between high-order-harmonic radiation from Ar and N_2 for the left-rotating harmonic components ($\Delta\phi_L$, blue squares) and right-rotating harmonic components ($\Delta\phi_R$, purple circles). (d) High-order-harmonic spectra from Ar-N_2 mixed gases for the left-rotating component (I_L, blue dash-dotted line) and right-rotating component (I_R, purple solid line), respectively. The laser parameters are the same as those in Fig. 3.

by an electron at infinite distance. $\mathbf{R}_j$ is the position of the nucleus; a_j and σ_j are the softening and the screening parameters. The TDSE is solved using the split-operator method. The initial state is obtained by solving TDSE with imaginary-time propagation, where the excited states are obtained by executing $\psi'(t) = \psi(t) - \sum_i \langle\psi_i|\psi(t)\rangle\psi_i$ after each time step. ψ_i represents the lower-energy eigenstates. The values of the parameters in Eq. (A3) are the same as in [68,69] to ensure that the obtained initial state, possessing the same symmetry as the HOMO of N_2, has the same ionization potential as that of the HOMO. Similarly, the atom is also modeled by an effective potential [39,70] with a soft-core parameter of 3.81874 to obtain the ionization potential $I_p = 0.5791$ a.u., which matches the ionization potential of Ar.

The results of the calculation with TDSE are shown in Fig. 10. The laser parameters are the same as those in Fig. 3. Comparing Figs. 3 and 10, one can see that the results based on TDSE agree qualitatively with those of the Lewenstein model.

[1] P. B. Corkum and F. Krausz, Nat. Phys. **3**, 381 (2007).

[2] F. Krausz and M. Ivanov, Rev. Mod. Phys. **81**, 163 (2009).

[3] I. Orfanos, I. Makos, I. Liontos, E. Skantzakis, B. Förg, D. Charalambidis, and P. Tzallas, APL Photon. **4**, 080901 (2019).

[4] J. Li, J. Lu, A. Chew, S. Han, J. Li, Y. Wu, H. Wang, S. Ghimire, and Z. Chang, Nat. Commun. **11**, 2748 (2020).

[5] J. Itatani, J. Levesque, D. Zeidler, H. Niikura, H. Pépin, J. C. Kieffer, P. B. Corkum, and D. M. Villeneuve, Nature (London) **432**, 867 (2004).

[6] Y. He, L. He, P. Wang, B. Wang, S. Sun, R. Liu, B. Wang, P. Lan, and P. Lu, Opt. Express **28**, 21182 (2020).

[7] L. Li, P. Lan, L. He, W. Cao, Q. Zhang, and P. Lu, Phys. Rev. Lett. **124**, 157403 (2020).

[8] X. Liu, P. Li, X. Zhu, P. Lan, Q. Zhang, and P. Lu, Phys. Rev. A **95**, 033421 (2017).

[9] L. Medišauskas, J. Wragg, H. van der Hart, and M. Yu. Ivanov, Phys. Rev. Lett. **115**, 153001 (2015).

[10] Á. Jiménez-Galán, G. Dixit, S. Patchkovskii, O. Smirnova, F. Morales, and M. Ivanov, Nat. Commun. **9**, 850 (2018).

[11] L. Barreau, K. Veyrinas, V. Gruson, S. J. Weber, T. Auguste, J. F. Hergott, F. Lepetit, B. Carré, J. C. Houver, D. Dowek, and P. Salières, Nat. Commun. **9**, 4727 (2018).

[12] A. D. Bandrauk and K.-J. Yuan, Mol. Phys. **114**, 344 (2016).

[13] P. B. Corkum, Phys. Rev. Lett. **71**, 1994 (1993).

[14] K. S. Budil, P. Salières, A. L'Huillier, T. Ditmire, and M. D. Perry, Phys. Rev. A **48**, R3437 (1993).

[15] P. Dietrich, N. H. Burnett, M. Ivanov, and P. B. Corkum, Phys. Rev. A **50**, R3585 (1994).

[16] N. H. Burnett, C. Kan, and P. B. Corkum, Phys. Rev. A **51**, R3418 (1995).

[17] P.-C. Huang, C. Hernández-Garcia, J.-T. Huang, P.-Y. Huang, L. Rego, C.-H. Lu, S.-D. Yang, L. Plaja, A. H. Kung, and M.-C. Chen, IEEE J. Sel. Top. Quantum Electron. **25**, 8800312 (2019), and references therein.

[18] H. Eichmann, A. Egbert, S. Nolte, C. Momma, B. Wellegehausen, W. Becker, S. Long, and J. K. McIver, Phys. Rev. A **51**, R3414 (1995).

[19] S. Long, W. Becker, and J. K. McIver, Phys. Rev. A **52**, 2262 (1995).

[20] D. B. Milošević, W. Becker, and R. Kopold, Phys. Rev. A **61**, 063403 (2000).

[21] D. B. Milošević and W. Becker, Phys. Rev. A **62**, 011403(R) (2000).

[22] A. Fleischer, O. Kfir, T. Diskin, P. Sidorenko, and O. Cohen, Nat. Photon. **8**, 543 (2014).

[23] O. Kfir, P. Grychtol, E. Turgut, R. Knut, D. Zusin, D. Popmintchev, T. Popmintchev, H. Nembach, J. M. Shaw, A. Fleischer, H. Kapteyn, M. Murnane, and O. Cohen, Nat. Photon. **9**, 99 (2015).

[24] K. M. Dorney, J. L. Ellis, C. Hernández-García, D. D. Hickstein, C. A. Mancuso, N. Brooks, T. Fan, G. Fan, D. Zusin, C. Gentry, P. Grychtol, H. C. Kapteyn, and M. M. Murnane, Phys. Rev. Lett. **119**, 063201 (2017).

[25] N. Zhavoronkov and M. Ivanov, Opt. Lett. **42**, 4720 (2017).

[26] G. Lambert, B. Vodungbo, J. Gautier, B. Mahieu, V. Malka, S. Sebban, P. Zeitoun, J. Luning, J. Perron, A. Andreev, S. Stremoukhov, F. Ardana-Lamas, A. Dax, C. P. Hauri, A. Sardinha, and M. Fajardo, Nat. Commun. **6**, 6167 (2015).

[27] S. Stremoukhov, A. Andreev, B. Vodungbo, P. Salières, B. Mahieu, and G. Lambert, Phys. Rev. A **94**, 013855 (2016).

[28] C. Zhai, R. Shao, P. Lan, B. Wang, Y. Zhang, H. Yuan, S. M. Njoroge, L. He, and P. Lu, Phys. Rev. A **101**, 053407 (2020).

[29] R. Shao, C. Zhai, Y. Zhang, N. Sun, W. Cao, P. Lan, and P. Lu, Opt. Express **28**, 15874 (2020).

[30] H. Yuan, L. He, S. M. Njoroge, D. Wang, R. Shao, P. Lan, and P. Lu, Ann. Phys. (Berlin) **532**, 1900570 (2020).

[31] N. Sun, X. Zhu, B. Wang, D. Wang, R. Shao, P. Lan, and P. Lu, Phys. Rev. A **101**, 053437 (2020).

[32] M. Z. Li, Y. Xu, G. R. Jia, and X. B. Bian, Phys. Rev. A **100**, 033410 (2019).

[33] O. Neufeld, D. Podolsky, and O. Cohen, Nat. Commun. **10**, 405 (2019).

[34] X. Liu, X. Zhu, L. Li, Y. Li, Q. Zhang, P. Lan, and P. Lu, Phys. Rev. A **94**, 033410 (2016).

[35] J. Levesque, Y. Mairesse, N. Dudovich, H. Pépin, J. C. Kieffer, P. B. Corkum, and D. M. Villeneuve, Phys. Rev. Lett. **99**, 243001 (2007).

[36] X. Zhou, R. Lock, N. Wagner, W. Li, H. C. Kapteyn, and M. M. Murnane, Phys. Rev. Lett. **102**, 073902 (2009).

[37] S. Eckart, M. Kunitski, M. Richter, A. Hartung, J. Rist, F. Trinter, K. Fehre, N. Schlott, K. Henrichs, L. P. H. Schmidt, T. Jahnke, M. Schöffler, K. Liu, I. Barth, J. Kaushal, F. Morales, M. Ivanov, O. Smirnova, and R. Dörner, Nat. Phys. **14**, 701 (2018).

[38] X. Xie, A. Scrinzi, M. Wickenhauser, A. Baltuška, I. Barth, and M. Kitzler, Phys. Rev. Lett. **101**, 033901 (2008).

[39] X. Zhang, X. Zhu, X. Liu, F. Wang, M. Qin, Q. Liao, and P. Lu, Phys. Rev. A **102**, 033103 (2020).

[40] D. Wang, X. Zhu, H. Yuan, P. Lan, and P. Lu, Phys. Rev. A **101**, 023406 (2020).

[41] B. Vodungbo, A. B. Sardinha, J. Gautier, G. Lambert, C. Valentin, M. Lozano, G. Iaquaniello, F. Delmotte, S. Sebban, J. Lüning, and P. Zeitoun, Opt. Express **19**, 4346 (2011).

[42] D. D. Hickstein, F. J. Dollar, P. Grychtol, J. L. Ellis, R. Knut, C. Hernández-García, D. Zusin, C. Gentry, J. M. Shaw, T. Fan, K. M. Dorney, A. Becker, A. Jaroń-Becker, H. C. Kapteyn, M. M. Murnane, and C. G. Durfee, Nat. Photon. **9**, 743 (2015).

[43] J. L. Ellis, K. M. Dorney, D. D. Hickstein, N. J. Brooks, C. Gentry, C. Hernandez-Garcia, D. Zusin, J. M. Shaw, Q. L. Nguyen, C. A. Mancuso, G. S. M. Jansen, S. Witte, H. C. Kapteyn, and M. M. Murnane, Optica **5**, 479 (2018).

[44] C. Hernández-García, C. G. Durfee, D. D. Hickstein, T. Popmintchev, A. Meier, M. M. Murnane, H. C. Kapteyn, I. J. Sola, A. Jaron-Becker, and A. Becker, Phys. Rev. A **93**, 043855 (2016).

[45] P. C. Huang, C. Hernández-García, J. T. Huang, P. Y. Huang, C. H. Lu, L. Rego, D. D. Hickstein, J. L. Ellis, A. Jaron-Becker, A. Becker, S. D. Yang, C. G. Durfee, L. Plaja, H. C. Kapteyn, M. M. Murnane, A. H. Kung, and M. C. Chen, Nat. Photon. **12**, 349 (2018).

[46] D. Azoury, O. Kneller, M. Krüger, B. D. Bruner, O. Cohen, Y. Mairesse, and N. Dudovich, Nat. Photon. **13**, 198 (2019).

[47] M. Lewenstein, P. Balcou, M. Y. Ivanov, A. L'Huillier, and P. B. Corkum, Phys. Rev. A **49**, 2117 (1994).

[48] P. Antoine, B. Carré, A. L'Huillier, and M. Lewenstein, Phys. Rev. A **55**, 1314 (1997).

[49] Z. Chang, Phys. Rev. A **70**, 043802 (2004).

[50] M. J. Frisch, G. W. Trucks, H. B. Schlegel, G. E. Scuseria, M. A. Robb, J. R. Cheeseman, G. Scalmani, V. Barone, B. Mennucci, G. A. Petersson, H. Nakatsuji, M. Caricato, X. Li, H. P. Hratchian, A. F. Izmaylov, J. Bloino, G. Zheng, J. L. Sonnenberg, M. Hada, M. Ehara, K. Toyota, R. Fukuda, J. Hasegawa, M. Ishida, T. Nakajima, Y. Honda, O. Kitao, H. Nakai, T. Vreven, J. A. Montgomery, Jr., J. E. Peralta, F. Ogliaro, M. Bearpark, J. J. Heyd, E. Brothers, K. N. Kudin, V. N. Staroverov, R. Kobayashi, J. Normand, K. Raghavachari, A. Rendell, J. C. Burant, S. S. Iyengar, J. Tomasi, M. Cossi, N. Rega, J. M. Millam, M. Klene, J. E. Knox, J. B. Cross, V. Bakken, C. Adamo, J. Jaramillo, R. Gomperts, R. E. Stratmann, O. Yazyev, A. J. Austin, R. Cammi, C. Pomelli, J. W. Ochterski,

R. L. Martin, K. Morokuma, V. G. Zakrzewski, G. A. Voth, P. Salvador, J. J. Dannenberg, S. Dapprich, A. D. Daniels, Ö. Farkas, J. B. Foresman, J. V. Ortiz, J. Cioslowski, and D. J. Fox, computer code GAUSSIAN09, Rev. D.01. (Gaussian, Inc., Wallingford, CT, 2009).

[51] X. Zhang, L. Li, X. Zhu, X. Liu, Q. Zhang, P. Lan, and P. Lu, Phys. Rev. A **94**, 053408 (2016).

[52] Anh-Thu Le, R. R. Lucchese, and C. D. Lin, Phys. Rev. A **82**, 023814 (2010).

[53] X. Zhu, M. Qin, Q. Zhang, Y. Li, Z. Xu, and P. Lu, Opt. Express **21**, 5255 (2013).

[54] J. B. Bertrand, H. J. Wörner, P. Salières, D. M. Villeneuve, and P. B. Corkum, Nat. Phys. **9**, 174 (2013).

[55] B. K. McFarland, J. P. Farrell, P. H. Bucksbaum, and M. Gühr, Phys. Rev. A **80**, 033412 (2009).

[56] T. Kanai, E. J. Takahashi, Y. Nabekawa, and K. Midorikawa, Phys. Rev. Lett. **98**, 153904 (2007).

[57] N. Wagner, X. Zhou, R. Lock, W. Li, A. Wüest, M. Murnane, and H. Kapteyn, Phys. Rev. A **76**, 061403(R) (2007).

[58] M. Qin, X. Zhu, Q. Zhang, W. Hong, and P. Lu, Opt. Express **19**, 25084 (2011).

[59] A. Etches, C. B. Madsen, and L. B. Madsen, Phys. Rev. A **81**, 013409 (2010).

[60] T. Kanai, E. J. Takahashi, Y. Nabekawa, and K. Midorikawa, Phys. Rev. A **77**, 041402(R) (2008).

[61] L. Wang, W. Zhu, H. Li, and Y. Zhang, J. Opt. Soc. Am. B **35**, A39 (2018).

[62] K. Amini, J. Biegert, F. Calegari, A. Chacón, M. F. Ciappina, A. Dauphin, D. K. Efimov, C. F. de Morisson Faria, K. Giergiel, and P. Gniewek, Rep. Prog. Phys. **82**, 116001 (2019).

[63] K. Yoshii, G. Miyaji, and K. Miyazaki, Phys. Rev. Lett. **106**, 013904 (2011).

[64] J. B. Bertrand, H. J. Worner, P. Hockett, D. M. Villeneuve, and P. B. Corkum, Phys. Rev. Lett. **109**, 143001 (2012).

[65] H. Stapelfeldt and T. Seideman, Rev. Mod. Phys. **75**, 543 (2003).

[66] B. K. McFarland, J. P. Farrell, P. H. Bucksbaum, and M. Gühr, Science **322**, 1232 (2008).

[67] A. Zaïr, M. Holler, A. Guandalini, F. Schapper, J. Biegert, L. Gallmann, U. Keller, A. S. Wyatt, A. Monmayrant, I. A. Walmsley, E. Cormier, T. Auguste, J. P. Caumes, and P. Salières, Phys. Rev. Lett. **100**, 143902 (2008).

[68] M. Peters, T. T. Nguyen-Dang, E. Charron, A. Keller, and O. Atabek, Phys. Rev. A **85**, 053417 (2012).

[69] X. Zhu, X. Liu, Y. Li, M. Qin, Q. Zhang, P. Lan, and P. Lu, Phys. Rev. A **91**, 043418 (2015).

[70] I. Barth and M. Lein, J. Phys. B **47**, 204016 (2014).